

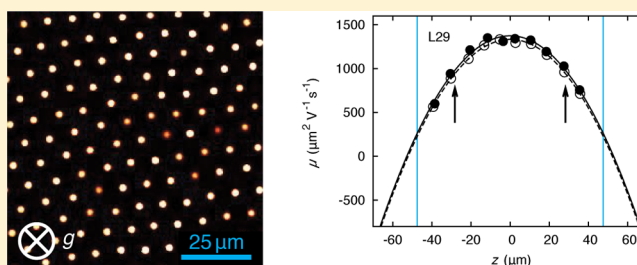
Charging of Poly(methyl methacrylate) (PMMA) Colloids in Cyclohexyl Bromide: Locking, Size Dependence, and Particle Mixtures

Marjolein N. van der Linden,^{*,†,‡} Johan C. P. Stiefelhagen,[†] Gülşen Heessels-Gürboğa,[†] Jessi E. S. van der Hoeven,[†] Nina A. Elbers,[†] Marjolein Dijkstra,[†] and Alfons van Blaaderen^{*,†}

[†]Soft Condensed Matter, Debye Institute for Nanomaterials Science, Princetonplein 5, 3584 CC, Utrecht, The Netherlands

S Supporting Information

ABSTRACT: We studied suspensions of sterically stabilized poly(methyl methacrylate) (PMMA) particles in the solvent cyclohexyl bromide (CHB; $\epsilon_r = 7.92$). We performed microelectrophoresis measurements on suspensions containing a single particle species and on binary mixtures, using confocal microscopy to measure the velocity profiles of the particles. We measured the charge of so-called locked PMMA particles, for which the steric stabilizer, a comb-graft stabilizer of poly(12-hydroxystearic acid) (PHSA) grafted on a backbone of PMMA, was covalently bonded to the particle, and for unlocked particles, for which the stabilizer was adsorbed to the surface of the particle. We observed that locked particles had a significantly higher charge than unlocked particles. We found that the charge increase upon locking was due to chemical coupling of 2-(dimethylamino)ethanol to the PMMA particles, which was used as a catalyst for the locking reaction. For particles of different size we obtained the surface potential and charge from the electrophoretic mobility of the particles. For locked particles we found that the relatively high surface potential ($\sim +5.1 k_B T/e$ or +130 mV) was roughly constant for all particle diameters we investigated ($1.2 \mu\text{m} < \sigma < 4.4 \mu\text{m}$), and that the particle charge was proportional to the square of the diameter.



1. INTRODUCTION

Suspensions of charged colloids are widely used as model systems to study the phase behavior of atomic and molecular systems.¹ They are also of interest for many technological and industrial applications.^{2,3} In the past decade, interest in interactions between charged particles in low- and apolar solvents and the origins of their charges has been rekindled because of the development of new model systems that can be used to explore soft potentials with a range significantly longer than the particle diameter, even for micron-sized colloids,^{4–9} as well as applications in several areas of advanced materials, such as electrophoretic displays,¹⁰ toner for printing and copying,¹¹ and electrorheological fluids.¹² Unfortunately, the charging mechanisms of particles in low- and apolar solvents are still poorly understood compared to those in water, despite an increasing number of efforts to understand these mechanisms,^{11,13–27} and they may differ for different particle systems. For a recent review on the charging mechanisms that involve charge control agents see ref 28.

In this work we performed electrophoresis measurements by means of confocal microscopy to investigate the surface potential and charge in systems of sterically stabilized charged colloids (poly(methyl methacrylate); PMMA) in a low-polar solvent (cyclohexyl bromide; CHB) at concentrations where the particles strongly interacted, including dispersions composed of colloidal crystals. The pair interaction in a system of

charged colloidal particles is commonly described by a hard-core repulsive Yukawa (screened Coulomb) potential^{4,5,29} (see Supporting Information (SI)). In a previous paper of our group the surface potential and charge were measured as a function of volume fraction¹⁵ in similar systems, but the effect of the particle size and mixtures of different particles were not investigated. In the current work we determined the surface potential and charge as a function of the particle diameter and for mixtures of particles. Such mixtures can be tuned to contain oppositely charged particles through addition of a salt such as tetrabutylammonium bromide (TBAB), which can reverse the surface charge on the particles from positive to negative, because slightly more bromide ions than cations adsorb onto the poly(12-hydroxystearic acid) (PHSA)–PMMA surface.^{30,31}

The solvent we used is a low-polar solvent, which means it has a relative dielectric constant in the range $\epsilon_r \approx 5–10$. Low-polar solvents have advantages over apolar solvents (for which $\epsilon_r \approx 2$), when used as a suspending medium for charged colloids. It can be shown (see SI and refs 2 and 13), for a monovalent salt, that the concentration (number density) of free ions can be approximated by

Received: September 12, 2014

Revised: December 2, 2014

Published: December 23, 2014

$$c_i \approx \sqrt{\frac{3c_0}{\pi a^3}} \exp\left(-\frac{\lambda_B}{2a}\right) \quad (1)$$

with c_0 the total concentration (number density) of salt, a the center-to-center distance of the dissociating ion pair, and λ_B the Bjerrum length.

In apolar solvents ($\epsilon_r \approx 2$) such as alkanes screening of electrostatic interactions is usually negligible and the creation of ions is energetically very unfavorable. A typical salt such as NaCl ($a \approx 0.28 \text{ nm}^{32}$) easily dissociates in water ($\epsilon_r = 80$, $\lambda_B = 0.7 \text{ nm}$ at $T = 295 \text{ K}$), but the concentration of free ions in the apolar solvent dodecane ($\epsilon_r = 2$, $\lambda_B = 28.3 \text{ nm}$) would be only $\sim 10^{-22} \text{ mol L}^{-1}$ for $c_0 = 0.01 \text{ mol L}^{-1}$ (from eq 1). This means that in apolar solvents so-called charge control agents are needed to arrive at sufficiently high ion concentrations to start modifying interparticle interactions. Usually, these charge control agents consist of a sizable alkyl chain and a more polar section to provide binding sites to the ions. This configuration makes these compounds in almost all cases (strongly) surface-active and the particle interactions strongly sensitive to (trace amounts of) water.²⁸

In low-polar solvents ($5 < \epsilon_r < 10$) such as cyclohexyl bromide ($\epsilon_r = 7.92$,³³ $\lambda_B = 7.1 \text{ nm}$ at $T = 298 \text{ K}$) the dissociation of ions is appreciably larger. The concentration of free ions can be further increased by using a salt consisting of large ions, for instance tetrabutylammonium bromide (TBAB; $a \approx 0.55 \text{ nm}^{34}$). For TBAB ($c_0 = 0.01 \text{ mol L}^{-1}$) in CHB eq 1 yields a total concentration of free ions $\sim 5 \times 10^{-4} \text{ mol L}^{-1}$. Thus, in low-polar solvent systems the double layers can still be very large (\sim tens of microns), but also made quite small (\sim nanometers) by addition of salts like TBAB.^{4,5,8,15} Furthermore, the charge and double-layer thickness are not very sensitive to water; water can even be used as ion exchange agent to remove salt.^{7,14}

In short, the use of low-polar solvents (with $5 < \epsilon_r < 10$) rather than apolar solvents (with $\epsilon_r \approx 2$) retains many of the desirable properties of apolar solvents (immiscibility with water, low conductivities, very large double layers), while ions are more easily created without surfactants and the system is less sensitive to small amounts of water.

Electrophoresis techniques that have been commonly used to study charged particles in low- and apolar solvents include phase analysis light scattering³⁵ and electroacoustic phoresis.²⁶ The recently increased interest in these systems resulted in the improvement of existing and development of new electrophoresis techniques. Most techniques measure the motion of single particles.^{15,17,18,23} Several make use of optical tweezers to confine the particles when they are driven by an electric field.^{13,17,23} Position determination at the single-particle level is done either using a photoquadrant detection scheme or by image processing.

Our approach makes use of confocal microscopy, which also allows measurements on individual particles in more concentrated systems, even in crystallized systems.¹⁵ Of course, for more concentrated systems it is harder to convert a measured mobility to a surface charge or potential than for dilute systems. The approach taken in this paper is the same as in earlier work by our group, in which a Poisson–Boltzmann cell model was used to obtain these quantities.¹⁵ Measurements at high volume fractions in systems with large relative screening lengths $(\kappa\sigma)^{-1}$ were also performed by the Palberg group using laser Doppler velocimetry. They studied polar systems for which a large

$(\kappa\sigma)^{-1}$ was achieved by using small particles^{36,37} rather than an extremely low ionic strength.

Despite significant progress, a lot is still unknown about the exact charging mechanisms in low- and apolar solvents, which is reflected in different approaches to explain them. Some groups try to relate the particle charge to the acid/base properties of the particles and thus relate the charging mechanism to behavior in water,^{25,38} while others look at hydrophilic/hydrophobic effects.²⁴ It is quite clear that most of the surfactant-like charge control agents enlarge the effective size of ions by micelle formation and thus enhance dissociation of ion pairs. However, details on how this enhanced ion pair dissociation in solution exactly charges the particles are less clear.^{13,18,21,28} It is important to mention that surfactants with nonionizable groups are just as effective in increasing conductivity and charging the particles in low-polar solvents as are ionic surfactants.²⁴ Also, as we already mentioned, all systems with charge control agents are sensitive to trace amounts of water,^{24,25,28} while the screening length of our PMMA particles in CHB is not sensitive to water; these suspensions can even be deionized effectively with water.^{7,14}

The charge on the PMMA particles in “pure” CHB is thought to arise from adsorption of protons and bromide ions, which result from decomposition of CHB. The dehalogenation reaction is not likely to be a simple equilibrium similar to the dissociation of water, which is generally not considered a decomposition of water. A slightly larger adsorption of protons then gives a positive charge (see ref 39 and chapter 2 of ref 14). When a salt with large ions such as TBAB is added to a solvent like CHB, significant dissociation takes place and the conductivity increases appreciably. In addition, the sign of the particle charge changes from plus to minus, which is thought to be due to an increased adsorption of bromide ions.^{5,8} In the course of our investigation, we noticed that so-called “locked” particles (for which the PHSA–g–PMMA–stabilizer chains were chemically linked to other PMMA chains in the particle) had a significantly higher particle charge than their “unlocked” counterparts. We investigated this phenomenon in more detail and found that the charge increase was presumably due to chemical attachment of the locking catalyst to the particle.

A constant surface charge density is only expected when the charge-determining ions arise from strongly dissociating salts or acids/bases in water. In all other cases some kind of association–dissociation equilibrium is operative at the surface of the particles and one expects a more complex relation for the surface potential of the particles as a function of size, volume fraction, and ionic strength. In the Supporting Information we provide the relation between surface potential and charge in the limit of low density and low surface potential. The simplest models predict a particle charge that scales with the particle surface area over a large parameter range.⁴⁰ For several systems with added surfactant-like charge control agents the surface potential was found to be independent of particle size.^{13,22} Complicated charge regulation mechanisms were required to provide explanations for these results.^{13,21,22} As mentioned, in our sterically stabilized PMMA system in CHB no charge control agents were used and it is therefore interesting to find out if the dependence of the surface potential on particle size was different than the examples from refs 13, 21, and 22.

2. EXPERIMENTAL METHODS

2.1. Model System. We used poly(methyl methacrylate) spheres (PMMA; density $d_{\text{PMMA}} = 1.19 \text{ g cm}^{-3}$; dielectric constant $\epsilon_r = 2.6$;

refractive index $n_D^{25} = 1.492^{14}$), synthesized by dispersion polymerization and sterically stabilized by a so-called comb-graft steric stabilizing layer formed by poly(12-hydroxystearic acid) (PHSA) grafted onto a backbone of PMMA (PHSA-*g*-PMMA).^{41,42} We used several batches of particles, of different mean diameter σ and labeled with either the fluorescent dye rhodamine isothiocyanate (RITC; see also SI) or the fluorescent dye 7-nitrobenzo-2-oxa-1,3-diazol (NBD). The mean diameters and polydispersities s were determined by static light scattering (SLS) or scanning electron microscopy (SEM). To determine the average diameter and size polydispersity from the SEM images we measured ~ 100 particles from each batch using the program iTEM (Olympus Soft Imaging Solutions GmbH). Some batches of particles underwent a so-called “locking” procedure,⁴³ in which the PHSA-*g*-PMMA stabilizer became covalently bonded to the particle surface (see SI); in the remainder of this paper, these particles are referred to as “locked”. In the case of “unlocked” particles, the PHSA-*g*-PMMA stabilizer is adsorbed to the particle surface, but not covalently bonded to it. The locking procedure was as follows.⁴¹ The particles were transferred to a solution of dodecane (~ 1.3 g/g PMMA) saturated with PHSA-*g*-PMMA stabilizer, which was made by thoroughly mixing 1 g of stabilizer with 20 mL of dodecane. The mixture was heated to 130 °C under stirring. A small amount (~ 4.2 $\mu\text{L/g}$ PMMA) of 2-(dimethylamino)ethanol (DMAE) was added as a catalyst and the mixture was stirred for 2 h at 130 °C. Finally, the particles were washed 3 \times with hexane.

The particles were suspended in cyclohexyl bromide (CHB; Sigma-Aldrich; density $d_{\text{CHB}} = 1.336$ g cm⁻³;¹⁴ dielectric constant $\epsilon_r = 7.92$;³³ refractive index $n_D^{25} = 1.4935^{14,33}$). As the refractive index of CHB nearly matched that of the PMMA particles, the van der Waals interactions are much smaller than $k_B T$ and can be neglected. The solvent CHB is known to decompose in time, a process which generates H⁺ and Br⁻ ions (see ref 39 and chapter 2 of ref 14). To reduce the ionic strength, we cleaned the solvent before use by bringing it into contact first with activated alumina (Al₂O₃; 58 Å, ~ 150 mesh, Sigma-Aldrich) and then with molecular sieves (4 Å, 10–18 mesh, Acros Organics). The conductivity of CHB after the cleaning steps was on the order of 10 pS cm⁻¹ (Scientifica 627 conductivity meter).

2.2. Sample Preparation. To measure the electrophoretic mobility of the particles in real space, we constructed electrophoresis sample cells in the following way (see also ref 15). A borosilicate glass capillary with inner dimensions length \times width \times depth = 5 cm \times 2.0 mm \times 0.10 mm ($x \times y \times z$; VitroCom) was mounted on a microscope glass slide with two thin strips of adhesive tape (Scotch). Two nickel alloy wires (T2 thermocouple alloy wire, Goodfellow; diameter = 0.05 mm) served as electrodes. The wires were bent in a rectangular U-shape and inserted into the capillary (one at each end) in such a way that the wires were typically ~ 2 cm apart. We stuck the wires to the glass slide with adhesive tape. For some measurements we used two straight wires parallel to the capillary wall, ~ 2.0 mm apart.

We prepared suspensions with an overall volume fraction $\eta \approx 0.02$. Each suspension was transferred to a separate electrophoresis cell using a glass Pasteur pipet. We checked that no air bubbles were present between the two electrodes. Both ends of the capillary were sealed with UV-curing optical adhesive (Norland no. 68). We prevented air bubbles at both ends of the capillary by tilting the capillary before applying the glue, such that any air was pushed out by the dispersion inside; the extra volume occupied by the glue also expelled the air from the other side of the capillary. Prior to the electrophoresis measurements the sample was homogenized on a rotating stage⁴⁴ by slowly rotating the capillary around its long axis for at least 1 h.

2.3. Electrophoresis Measurements. For each sample we obtained the particle mobility in the following way. We applied a DC electric field and measured the mean particle velocity as a function of depth (total depth = 0.10 mm) in the capillary. The velocities were converted to apparent mobilities (eq 2, below) and from a fit to the mobility profile we obtained the mean particle mobility (the mean apparent particle mobility at the stationary level). We used a wideband amplifier (Krohn-Hite, model 7602M) to apply DC fields of 2–8 V

mm⁻¹ in both directions. Typically, we measured two mobility profiles for the same sample, using two different field strengths, to check whether the measured mobility was independent of the field strength.

In most cases the long axis of the capillary and the electric field direction were parallel to the direction of gravity to prevent a density gradient across the 0.10-mm depth due to sedimentation of the particles. We corrected for the effect of gravity on the apparent particle mobility, as described below (Section 2.5).

2.4. Confocal Microscopy. Particle imaging was performed with confocal microscopy with an oil immersion objective (100 \times NA 1.4, 63 \times NA 1.4, or 40 \times NA 1.25, Leica), in fluorescence mode with 532 nm, 543 nm (both RITC), and 488 nm (NBD) excitation. We mostly used a Nipkow spinning-disk confocal microscope (CSU10, Yokogawa) in combination with a digital video camera (Evolution QEi). In some cases we used a Leica SP2 or Nikon C1 confocal microscope. We obtained series of images (~ 20 –50 images; typical image size 50 $\mu\text{m} \times 50 \mu\text{m}$; pixel size 0.23–0.45 μm ; time interval between two frames 0.03–0.7 s) at several depths (typically ~ 10 positions across the 0.10-mm total depth). In most cases we took series of 2D images at different depths; in a few cases we took series of 3D image stacks. Typically, we changed the field direction after each series of images or image stacks.

2.5. Electrophoretic Mobility. We obtained the 2D trajectories of the particles using an algorithm described by Vissers et al. in ref 15, based on the 2D tracking code as described in ref 45. Typically, for each series of images, we determined the trajectories of 10–50 particles, which could be followed in at least five consecutive frames. From the particle trajectories we calculated the (mean) apparent mobility of the particles (see above) in the direction of the electric field as a function of depth z in the capillary (mobility profile), given by

$$\mu(z) = v(z)/E \quad (2)$$

with $v(z)$ the (mean) particle velocity (m s⁻¹) in the direction of the electric field at a certain depth z and E the field strength (V m⁻¹). The particle velocity is the sum of the fluid velocity (electro-osmotic flow velocity) at depth z and the particle velocity v_E with respect to the fluid as a result of the applied field; the corresponding particle mobility is $\mu_E = v_E/E$.

We fitted the mobility profile with a parabolic function. For samples for which the direction of the electric field was parallel to the direction of gravity, we either averaged $\mu(z)$ for the two different field directions, or fitted with an extra fit parameter, a constant correcting for the sedimentation velocity.

We set $z = 0$ to correspond to the maximum of the parabolic profile and the middle of the capillary. At the stationary levels (at depth $z = z_{\text{stat}}$), where the electro-osmotic flow was assumed to be zero, we could obtain the particle mobility $\mu_E = \mu(z_{\text{stat}})$. The stationary levels in a rectangular cell are located at⁴⁰

$$\frac{z_{\text{stat}}}{h} = \pm \sqrt{\frac{1}{3} + 4 \left(\frac{2}{\pi}\right)^5 \frac{1}{k}} \quad (3)$$

where h is half the depth of the channel and k is the ratio between the long and short cross-sectional distances (width and depth) of the channel.

2.6. Surface Potential and Charge. An estimate for the Debye screening length κ^{-1} was obtained from the measured conductivity of the solvent CHB (see SI). We used the theory of Carrique et al.⁴⁶ to obtain the dimensionless surface potential $\beta e \psi_0$ and charge number Z from the measured mobility. In this theory a Kuwabara cell model is used to calculate ψ_0 and Z from the measured mobility μ for any given screening length κ^{-1} and volume fraction η by numerically solving the full Poisson–Boltzmann equation; the double layers are allowed to overlap. In ref 15 the theory was used to relate the mobility to $\beta e \psi_0$ and Z for a system similar to our systems. As for our systems the plane of shear is close to the particle surface (at a distance of ~ 10 nm, the thickness of the steric stabilizing layer), the electrostatic surface potential ψ_0 may be assumed to be similar to the zeta potential.^{14,40}

Table 1. Summary of the Electrophoresis Results for Locked and Unlocked PHSA-*g*-PMMA-Stabilized PMMA Particles in CHB (See Text for Details)^a

sample	particle	single/mixture	$\sigma/\mu\text{m}$	s (%)	dye	locked	$E/(\text{V mm}^{-1})$	η	state	$\mu_E/(10^2 \mu\text{m}^2 \text{V}^{-1} \text{s}^{-1})$	$\beta\omega\gamma_0$	Z
1*	L12	s	1.18	4.0	RITC	yes	2.6	0.032	F	10.9	6.77	438
2*	L12	s	1.18	4.0	RITC	yes	2.5, 3.5	0.027	F	8.43±0.02	5.73±0.01	296±1
3*	L19	s	1.92	3.1	NBD	yes	2.5, 3.5	0.014	X	12.7±0.3	5.17±0.09	653±20
4*	L20	s	1.98	3.5	NBD	yes	2.4, 3.4	0.018	X	8.7±0.3	4.24±0.10	456±19
5*	L20	s	1.98	3.5	NBD	yes	2.4, 3.3	0.011	X	13.5±0.4	5.06±0.13	688±29
6	L20	m	1.98	3.5	NBD	yes	2.5, 3.5	0.028	F	13.8±0.3	6.5±0.1	1015±40
6	U16	m	1.58	3.5	RITC	no	2.5, 3.5	0.028	F	3.5±0.2	3.29±0.09	153±9
7*	L22	s	2.23	3.6	NBD	yes	2.3, 3.2	0.031	F	8.3±0.3	4.60±0.08	579±21
8*	L29	s	2.87	2.4	NBD	yes	2.5, 3.4	0.006	X	13.9±0.4	3.77±0.12	896±36
9*	L44	s	4.36	2.8	NBD	yes	2.6, 3.7	0.005	X	21.3±1.1	5.44±0.41	2960±400
10	U16	s	1.58	3.5	RITC	no	2.5, 3.5	0.02	F	5.89±0.04	3.85±0.01	242±2
11	U20	s	1.98	3.5	NBD	no	3.5, 7.4, 7.4	0.02	F	5.6±1.0	3.29±0.38	290±56

^aValues from the samples marked with an asterisk (*) were used to create the plots in Figure 2. Mobility profiles for all samples can be found in the SI.

3. RESULTS AND DISCUSSION

3.1. Mobility Profiles. Typically, we measured two mobility profiles for each sample, at two different field strengths (see Table 1). We did not find a significant dependence of the mobility on the field strength. All measured mobility profiles on which the electrophoresis results in Table 1 were based are included in the Supporting Information. The given errors are the standard deviation of the measurements on the same sample; they serve as a rough indication of the measurement error.

It is important to note that most samples containing one-component suspensions of locked particles (samples 3–5, 8, 9) were crystalline before and also during the electrophoresis measurements. No shear melting of the crystals took place during the measurements. Because the velocity of the particles during the measurements depended on the distance from the wall, the 3D crystalline order could not be preserved. Instead, during the measurements the crystalline samples consisted of sliding 2D crystalline layers. Three samples containing one-component suspensions of locked particles were not crystalline, but fluid (samples 1, 2, and 7), by which we mean that there was no crystalline order (3D or 2D). Samples of composition similar to that of sample 7 were usually crystalline, indicating that the particle charge and/or Debye screening length varies between the samples even though they were prepared in the same way. The remaining samples (6, 10, and 11), which contained a mixture or a one-component suspension of unlocked particles, were fluid. Because the mobility profiles for all samples, including the crystalline samples, could be well fitted with a parabolic function (SI), we assumed in all cases that the stationary levels were located at $z = z_{\text{stat}}$ and that $\mu_E = \mu(z_{\text{stat}})$, as explained above (Section 2.3).

We observed shear-melting twice, for two samples containing a one-component suspension with L20 (partial shear-melting) or L29 particles (full shear-melting). The measurements for these samples were performed at relatively high field strengths of $E = 7.6$ and 7.7 V mm^{-1} , respectively, corresponding to typical energies on the particle length scale of the order of $Ze \times E \times \sigma = 10^3 k_B T$, which illustrates how far the systems were brought out of equilibrium by the external electric field (see also refs 30, 31.). Although the resulting mobility profiles looked parabolic, analysis of the results yielded unphysically high values for the surface potential and charge. This most likely was due to the measurements being performed in the

nonlinear regime, where the particle velocity is not linearly dependent on the electric field strength. The results were therefore not included in Table 1.

Some of our findings are different from observations of Medebach and Palberg³⁶ in systems of polystyrene particles in water with $\sigma = 136 \text{ nm}$, $(\kappa\sigma)^{-1} \approx 5$ and a volume fraction of a few percent; they found a distinct difference between the shape of the mobility profile for colloidal crystals and that for fluids or melts (shear-molten crystals). In their case, the profile for fluids and melts had the expected parabolic shape, whereas the profile for colloidal crystals was a flattened parabola at the start of the measurement and became completely flat (plug-like motion) on the time scale of a second. In contrast, we observed parabolic profiles for both fluid and crystalline samples, despite the fact that our measurements typically took ~ 30 seconds to several minutes. Furthermore, Medebach and Palberg observed shear melting of the colloidal crystals above a critical field strength, which increased with volume fraction (from $E \approx 3.5 \text{ V mm}^{-1}$ for $\eta \approx 0.0076$ to $E \approx 4.6 \text{ V mm}^{-1}$ for $\eta \approx 0.0090$). We also observed shear melting twice, for measurements that were performed at relatively high field strengths of $E = 7.6$ and 7.7 V mm^{-1} . We note that Medebach and Palberg³⁶ used particles with a diameter of 136 nm , 9–32 times smaller than our particles with $\sigma = 1.18$ – $4.36 \mu\text{m}$. In a later paper, Medebach et al.³⁷ reported that, despite the nonparabolic mobility profiles they found for colloidal crystals, the measured electrophoretic mobility seemed to be a single-particle property, not influenced by the structural state of the suspensions (fluid or crystal).

Our results show that it is possible to perform electrophoresis measurements on samples with sliding 2D crystalline layers without melting (i.e., disappearance of 2D crystalline order) taking place during the measurement and that parabolic flow profiles can be obtained for those crystalline samples.

3.2. Surface Potential and Charge. Table 1 summarizes the electrophoresis results. For each sample we report the suspension properties: the name of the particle, whether the measurements were done in a one-component suspension or in a mixture, the mean diameter σ , and polydispersity s of the particles as determined by static light scattering (SLS; particles L12 and U16, samples 1, 2, 6, and 10) or scanning electron microscopy (SEM; all other particles), the type of fluorescent dye used to label the particle, and whether the particle was locked or unlocked. These are followed by the field strengths E at which the measurements were performed, the volume

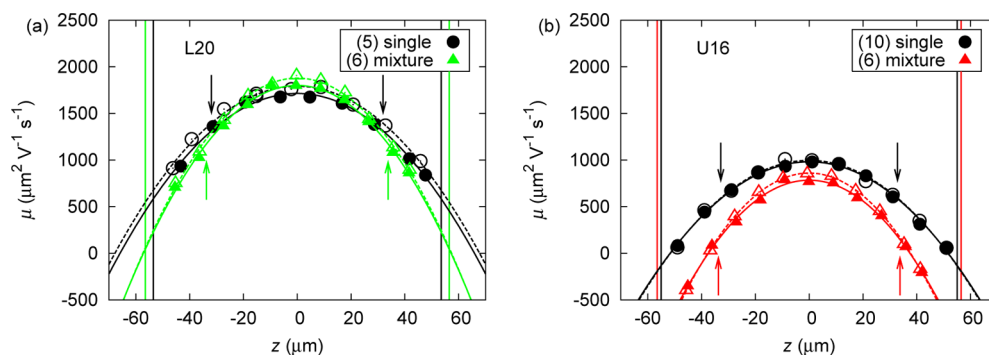


Figure 1. Mobility profiles for locked and unlocked PHSA-*g*-PMMA-stabilized PMMA particles in CHB. (a) Locked particles (L20, samples 5 and 6) and (b) unlocked particles (U16, samples 10 and 6), measured in a one-component suspension (black circles) and for the particles in the (same) binary mixture (green or red triangles). The vertical lines in each panel indicate the positions of the walls, the arrows indicate the two stationary levels (where the electro-osmotic flow is zero; $z = z_{\text{stat}}$; eq 3). The data and fits have been corrected for the contribution of gravity to the apparent mobility of the particles (see Section 2.3). Experimental details for these samples are in Table 1. The profiles for all samples reported in Table 1 can be found in the Supporting Information.

fraction η of the suspension, and the state of the suspension during the measurements ($X = \text{crystalline}$, $F = \text{fluid}$). Finally, in the last three columns of Table 1, we report the results: the mean particle electrophoretic mobility μ_E as determined by electrophoresis, the dimensionless surface potential $\beta\psi_0$ ($T = 298 \text{ K}$), and the number of charges on the particle Z . The latter two were calculated from μ_E , assuming a Debye screening length κ^{-1} of $6 \mu\text{m}$. The errors reported for μ_E , $\beta\psi_0$, and Z are the standard deviations of multiple measurements for the same sample and thus are not available for sample 1, for which only one measurement was performed.

The samples did not all have exactly the same volume fraction (Table 1), but the volume fractions are in the range where no significant dependence of the charge on the volume fraction is expected.¹⁵ The volume fraction reported for sample 6 is the total volume fraction of L20 and U16 particles.

The electrophoretic mobility μ_E was obtained from a parabolic fit to the mobility profiles as described in Section 2.3. We used the theoretical approach of ref 46 to calculate the dimensionless surface potential $\beta\psi_0$ and charge number Z from μ_E , using the values for η specified in Table 1 and $\kappa^{-1} = 6 \mu\text{m}$. All entries in Table 1 apply to one-component suspensions, except for those corresponding to sample 6, a mixture of particles L20 and U16, which will be discussed below (Section 3.3). The theory of ref 46 took into account the effects of overlapping double layers, which resulted in higher values for $\beta\psi_0$ and Z than would follow from assuming a negligible double-layer overlap.¹⁵

The variation in $\beta\psi_0$ and Z between two samples of similar composition can be quite large, much larger than the error estimated from measurements on the same sample, as we see from the two samples containing L12 (samples 1 and 2) and the two samples containing L20 (samples 4 and 5). The volume fractions were different in these samples, but this should not have a large effect on the charge, as was shown in ref 15 for a system similar to our systems. Moreover, there seems to be no systematic dependence of the charge on the volume fraction. However, the samples were made at different points in time, with different dispersions, prepared from different batches of cleaned CHB. Also, we note that the electrophoresis cell was constructed separately for each sample, each time using a new capillary and new electrodes. These circumstances apparently affected the surface potential and charge of the particles.

All particles in Table 1 were found to be positively charged, from the direction of movement when the electric field was applied, in agreement with earlier work on similar systems.^{4,15} Electrophoresis measurements in previous work on similar systems (PMMA particles in CHB/*cis*-decalin) indicated that the type of dye did not significantly influence the charge (see chapter 2 of ref 14 and also SI). However, we observed that the chemical attachment of the comb-graft PHSA-PMMA steric stabilizer to other PMMA chains of the particle (locking) had a profound influence on the charge density of the particles. Locked particles clearly had higher surface potentials and charges than unlocked particles. This general trend is clearly illustrated by comparison of particles L20 (samples 4 and 5) and U20 (sample 11). Particle L20 was obtained by locking a batch of particle U20. The surface potential and charge of particle L20 were significantly higher than those of particle U20. We investigated the charge increase upon locking in more detail. In Section 3.5 we show that the catalyst 2-(dimethylamino)ethanol (DMAE), used in the locking step, attached to the particle by chemical bonding, thereby adding binding sites for H^+ ions to the particle and increasing the (positive) charge of the particles.

Samples 10 and 11, containing unlocked particles, were in the fluid state, which is consistent with their lower surface potential and charge density compared to the locked particles. We see this from the constant-potential and charge-regulation phase diagrams in ref 47 (for $\lambda_B/\sigma = 0.005$): a system with $(\kappa\sigma)^{-1} \approx 3$ and $\eta = 0.02$ (approximately as for our samples) is expected to be crystalline with bcc symmetry if $\beta\psi_0 = 5$, but to be fluid when the surface potential is $\beta\psi_0 = 3$. Samples 1, 2, and 7, containing locked particles and having a potential close to $\beta\psi_0 = 5$ or higher, were also in the fluid state. We see from ref 47 that this could be due to the relatively high volume fractions of these samples. For certain combinations of parameters $\beta\psi_0$ and $(\kappa\sigma)^{-1}$ re-entrant melting is expected to occur, as was observed experimentally in our group before.^{39,44} For example, for $\lambda_B/\sigma = 0.005$, $\beta\psi_0 = 5$ and $(\kappa\sigma)^{-1} \approx 4.1$, a fluid is stable for $\eta \gtrsim 0.031$.⁴⁷

On the basis of the bare charges in Table 1, we can estimate the concentration of counterions in the Wigner-Seitz cell, which is up to two orders of magnitude larger than the background concentration of ions estimated from the measured conductivity of purified CHB ($2.4 \times 10^{-10} \text{ mol L}^{-1}$). It would therefore be interesting to investigate in future work whether

the theory can be modified to incorporate this by allowing the screening length to vary.

3.3. Binary Mixture. In Figure 1 we plotted two mobility profiles for two one-component samples (samples 5 and 10; filled and open black circles), containing particles L20 and U16, respectively. We also measured the mobility profiles for the same particles in a binary mixture 1 day after mixing. The green and red triangles in Figure 1a and b correspond to particles L20 (green) and U16 (red), respectively, in the binary mixture (sample 6). For each sample two profiles were measured, at different field strengths, $\sim 2.5 \text{ V mm}^{-1}$ (filled circles or triangles) and 3.5 V mm^{-1} (open circles or triangles). The vertical solid lines indicate the positions of the walls. The two stationary levels (where the electro-osmotic flow is zero; $z = z_{\text{stat}}$; eq 3) have been indicated by arrows. The mobility of the particle is given by the value of the mobility profile at the position of the stationary levels. We see that the two profiles measured at different field strengths in each case give almost the same value for the particle mobility.

The values of $\beta e \psi_0$ and Z for particles L20 and U16 in the mixture (sample 6) are somewhat higher and lower, respectively, than the same values in samples 4 and 5 (L20) and 10 (U16) (Table 1). This could be due to charge regulation effects between the two different species. We also note that the theory of ref 46 is valid for one-component suspensions and might not be accurate for the binary mixture of sample 6. Although we can therefore not be sure of the precise values for $\beta e \psi_0$ and Z in the binary mixture, we can draw the following conclusions from the mobility profiles. First, both particles were positively charged, because they both moved in the same direction across almost the entire depth of the capillary. Only very close to the wall did the smaller particles move in the opposite direction. At the location of stationary level the smaller particles moved in the same direction as the larger particles, indicating that both particles were positively charged. Second, the charge on the smaller U16 particles was lower than the charge on the larger L20 particles, as the smaller particles had a smaller apparent mobility at all depths.

3.4. Size Dependence of Surface Potential and Charge. Figure 2a and b show, for the locked particles, the dimensionless surface potential $\beta e \psi_0$ and charge number Z , respectively, as a function of the diameter of the particles σ . We plotted the data for samples 1–5 and 7–9 (marked with an asterisk in Table 1), corresponding to particles L12 (2 \times), L19, L20 (2 \times), L22, L29, and L44. All these samples contained locked particles with diameters in the range 1.18–4.36 μm . Samples 3, 5, 7, 8, and 9 were prepared using the same batch of purified CHB. The values for $\beta e \psi_0$ (red squares in Figure 2a) and for Z (red squares in Figure 2b) corresponding to $\kappa^{-1} = 6 \mu\text{m}$, were taken from Table 1. To show what the effect is of using different estimates for κ^{-1} , we also included $\beta e \psi_0$ and Z values, obtained from a similar cell model calculation carried out for $\kappa^{-1} = 4 \mu\text{m}$ (green triangles pointing down) and $8 \mu\text{m}$ (blue triangles pointing up). In general, assuming a smaller screening length yields a smaller $\beta e \psi_0$ (Figure 2a) and a larger Z (Figure 2b). For the smaller particles, varying the estimate for κ^{-1} in the range 4–8 μm has little effect on the calculated charge. For the largest particle, the effect can be quite substantial, especially when lowering the estimate of κ^{-1} (the data point for Z corresponding to $\kappa^{-1} = 4 \mu\text{m}$ for the largest particle is off the scale of the graph in Figure 2b).

Figure 2a shows that, despite large variations between different samples, there is no systematic dependence on the

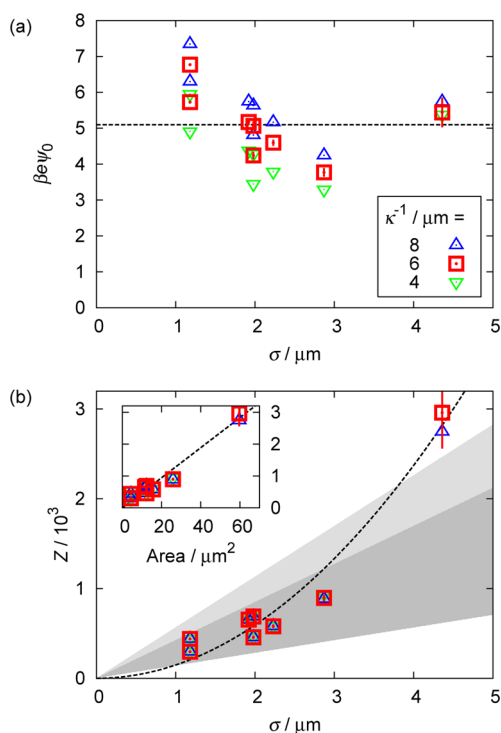


Figure 2. Surface potential and charge number versus diameter for locked PHSA-g-PMMA-stabilized PMMA particles in CHB for different estimates of the Debye screening length κ^{-1} . (a) Dimensionless surface potential $\beta e \psi_0$ versus diameter σ . The dashed line is the fit result $\beta e \psi_0 = 5.1 \pm 0.3$. (b) Charge number Z versus diameter σ ; inset: charge number Z versus the surface area $\pi \sigma^2$ of the particles. The dashed line is the fit result, corresponding to a surface charge density of $47 \pm 3 \text{ e } \mu\text{m}^{-2}$. Error bars (shown for $\kappa^{-1} = 6 \mu\text{m}$) correspond to the errors given in Table 1 and are only clearly visible for the largest particle; for all other particles the error bars are smaller than the point size. The gray shaded areas indicate possible charge renormalization regimes. See text for details.

particle size. Therefore, the surface potential can be considered approximately constant, independent of the size of the particle. This is in agreement with results of Roberts et al.,¹³ who also found a size-independent surface potential; however, in their case in a system with added surfactants to control the charge. A fit to our data for $\kappa^{-1} = 6 \mu\text{m}$ resulted in $\beta e \psi_0 = 5.1 \pm 0.3$ (for $\kappa^{-1} = 4$ and $8 \mu\text{m}$ the fits gave $\beta e \psi_0 = 4.4 \pm 0.3$ and 5.6 ± 0.3 , respectively).

In Figure 2b we see that the data points of Z versus σ can be approximated by a parabolic fit of the form $y = ax^2$, which is also plotted in the figure, suggesting a roughly constant surface charge density on the particles ($Z \propto \sigma^2$), for this range of particle diameters. The inset of Figure 2b makes this more clear. Here, we show Z as a function of the surface area of the particle, given by $\pi \sigma^2$. The line plotted through the data is a linear fit to the data. The slope is equal to the surface charge density divided by the elementary charge e , and corresponds to a surface charge density of $47 \pm 3 \text{ e } \mu\text{m}^{-2}$ ($57 \pm 4 \text{ e } \mu\text{m}^{-2}$ and $45 \pm 2 \text{ e } \mu\text{m}^{-2}$ for $\kappa^{-1} = 4$ and $8 \mu\text{m}$, respectively). Our results for the surface potential and surface charge density are comparable to values measured in ref 15, for systems of PMMA particles ($\sigma \approx 1 \mu\text{m}$) in CHB/*cis*-decalin with $\epsilon_r = 5.6$ for the solvent mixture and $(\kappa \sigma)^{-1} \approx 1$, and to values obtained in ref 48 for PMMA colloids ($\sigma = 1.66 \mu\text{m}$) in a mixture of cycloheptyl bromide and decalin by comparing measured radial

Table 2. Overview of Treatment, Phase Behavior, and Electrophoresis Results of Six Different Batches of PMMA Particles^a

batch	particle	treatment	conditions	catalyst	sedimentation			electrophoresis	
					sediment height (μm)	state	η	$\beta e\psi_0$	Z
1	U29	unlocked			11	F	0.015	-2.12 ± 0.06	-280 ± 9
2	L29	locked	2 h@130 °C	DMAE	100	X	0.012	$+4.04 \pm 0.07$	$+688 \pm 18$
3	H29	heated	2 h@130 °C		< 5	F	0.015	-1.76	-223
4	S29	stirred	2wks@25 °C	DMAE (10 \times)	16	F+X	0.018	$+3.59 \pm 0.00$	$+536 \pm 0$
5	T29	TEA	2 h@130 °C	TEA	< 5	F	0.008	-0.40 ± 0.00	-59 ± 0
6	N21	5% DMAE-MA			100	X	0.015	$+3.23 \pm 0.06$	$+266 \pm 8$

^aBatches 1–5 originated from the same synthesis batch, but after synthesis each batch received a different treatment. Batch 6 was synthesized using a monomer mixture containing 5 wt % 2-(dimethylamino)ethyl methacrylate (DMAE-MA) monomer. From left to right we report: the batch number, the particle name, the treatment name, the reaction conditions during the heating or stirring (if applicable), and the catalyst (if present). These data are followed by the results from the sedimentation study: the sediment height and the state of the suspension in CHB (F = fluid, X = crystalline) 2–3 h after sample preparation. Finally, we report the results from the electrophoresis measurements: the volume fraction during the electrophoresis measurements, the dimensionless surface potential $\beta e\psi_0$ ($T = 298$ K), and the charge number Z , measured in a solvent mixture of CHB and 20 wt % *cis*-decalin, assuming a Debye screening length κ^{-1} of 6 μm . Corresponding confocal images are in Figure 3.

distribution functions with those from Monte Carlo simulations (in ref 15 for $\eta \lesssim 0.04$: $\beta e\psi_0 \approx 3$ –4 and surface charge density $\sim 80 e \mu\text{m}^{-2}$; in ref 48 $\sim 28 e \mu\text{m}^{-2}$). We note that the quadratic dependence of Z on σ relies heavily on the data point at $\sigma = 4.36 \mu\text{m}$ (sample 9). Excluding this data point would result in a linear relation between Z and σ .

For particles with a high charge the interactions between two particles at some distance from each other can still be described by the Yukawa potential, but with the bare charge replaced by a (smaller) renormalized charge.^{29,49} At low bare charge the renormalized charge is equal to the bare charge, but as the bare charge increases the renormalized charge increases less and eventually, in the saturated charge regime, levels off to a plateau value. The saturated charge number Z_{sat} is proportional to the particle diameter.

Alexander et al. proposed the relation $Z_{\text{sat}} = A\sigma/\lambda_{\text{B}}$ for the saturated charge.²⁹ In experiments,^{49,50} simulations,⁵¹ and theoretical approaches without^{29,52} or including^{53,54} charge regulation, the proportionality constant A was found to depend on the volume fraction η and the salt concentration c_s . Experiments,⁵⁰ simulations,⁵¹ and two theoretical approaches, using the Poisson–Boltzmann cell model and the jellium model,^{29,55,52} all found $A \approx 3$ –4.5 for the volume fraction range 10^{-3} – 10^{-2} . In accordance with these values, we made the lines corresponding to $A = 3$ and 4 the upper bounds of the dark gray and light gray shaded area, respectively.

The dark gray shaded area in Figure 2b is bound on the lower side by the line $Z = \sigma/\lambda_{\text{B}}$ and on the upper side by the line $Z = Z_{\text{sat}} = 3\sigma/\lambda_{\text{B}}$. The light gray shaded area is bound on the upper side by the line $Z = Z_{\text{sat}} = 4\sigma/\lambda_{\text{B}}$. The lower bound of the dark gray area indicates above which charge renormalization effects become relevant.^{50,56} The upper bound is an indication of the maximum charge (saturated charge Z_{sat}) a particle can acquire^{52,56} when charge renormalization is taken into account.

The shaded areas thus indicate possible renormalization regimes for the particle charge. As the theory in ref 46, which we used to obtain $\beta e\psi_0$ and Z from the mobility, employs the nonlinearized Poisson–Boltzmann (PB) theory, the corresponding charges are *not* renormalized charges. The renormalized charges would follow from matching the linear to the nonlinear PB solution at the cell boundary⁵⁵ and are expected to saturate at a value Z_{sat} when the bare charge (i.e., the charge that follows from the nonlinear PB solution) exceeds this value. The bare charge for all particles is in or above the renormalization regime (gray areas) and therefore the

renormalized charge is expected to be lower than the reported bare charge.

3.5. Origin of Charge Increase upon Locking. As described in Section 3.2, we found that locked particles had higher surface potentials and charges than unlocked particles. It seemed probable that the locking procedure affected the surface chemistry of the particles, changing the adsorption equilibria of ions on the surface, and thereby increasing the surface charge density. We hypothesized that some 2-(dimethylamino)ethanol (DMAE), which was added during the locking step as a catalyst (see Section 2.1), attached to the particle either by adsorption or by the formation of covalent bonds. DMAE has a basic amino group, which can bind H^+ ions. Adsorption or covalent bonding of DMAE would therefore add binding sites for H^+ ions to the particles and explain the increase of (positive) charge.

One possible mechanism for the attachment of DMAE to the particles is adsorption on the particle surface or inside the bulk of particles. Another possible mechanism is covalent bonding of DMAE to PMMA. Our PMMA contains a small fraction (~ 3 wt %) of methacrylic acid (MAA) monomers, which are added to provide carboxylic acid groups for chemical linking of the steric stabilizer.^{41–43} DMAE has an alcohol group that possibly reacted with the carboxylic acid groups of the MAA monomers present in PMMA, forming an ester bond (see SI).

To test our hypothesis, we prepared suspensions of six different batches of PMMA particles for which we measured the charge and studied the phase behavior (sediment height and structure). Batches 1–5 originated from the same synthesis batch, but after synthesis each batch received a different treatment (see Table 2). Batch 6 was prepared in a separate synthesis.

Batches 1 and 2 contained unlocked particles (U29) and locked particles (L29), respectively. To find out whether DMAE was responsible for the charge increase, we performed the locking procedure (batch 3, H29) as described above (Section 2.1), but without the catalyst DMAE. To find out whether covalent bonding played a role, we performed the following three tests. For the first test (batch 4, S29) we prepared a reaction mixture similar to that used for locking the particles, only this time the DMAE concentration was 10 times higher, the particles were not heated, just stirred, and for a longer period of 2 weeks. We checked the behavior of the suspension after different durations of stirring. For covalent bonding (chemisorption) an activation energy barrier exists,

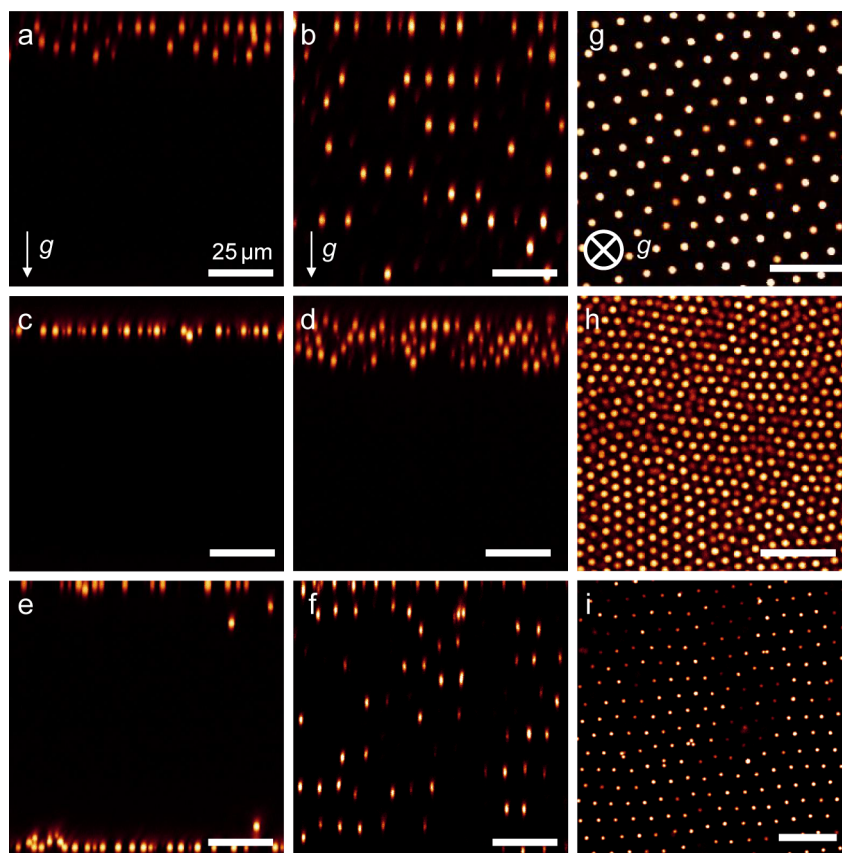


Figure 3. Confocal images corresponding to batches 1–6 in Table 2. Samples were prepared using suspensions of particles from batches 1–6 in cyclohexyl bromide (CHB) at a volume fraction $\eta \approx 0.02$. Images were taken 2–3 h after sample preparation. (a–f) xz Images of (a) U29, batch 1; (b) L29, batch 2; (c) H29, batch 3; (d) S29, batch 4; (e) T29, batch 5; (f) N21, batch 6. (g–i) xy Images of (g) L29, batch 2; (h) S29, batch 4, second layer from wall; (i) N21, batch 6. Scale bars represent 25 μm .

while for adsorption (physisorption) there is no energy barrier.⁵⁷ Therefore, if attachment of DMAE took place by covalent bonding, we would expect a dependence of the rate of charge increase on the temperature. In case of adsorption as the dominant mechanism, we would not expect a (strong) temperature dependence.

For the second test (batch 5, T29) we performed the same locking procedure as described above (Section 2.1), but instead of DMAE we used triethylamine (TEA) as a catalyst. TEA is similar to DMAE in the sense that TEA also has a tertiary amino group, which can bind H^+ . Therefore, if attachment of the catalyst took place by adsorption, we would find a similar charge increase for T29 as for L29. In contrast to DMAE, TEA does not have an alcohol group and therefore cannot form an ester bond with MAA. If attachment of the DMAE took place by covalent bonding, we would not find a similar charge increase for TEA.

The proposed esterification reaction between the MAA monomers and DMAE converts MAA monomers into 2-(dimethylamino)ethyl methacrylate (DMAE-MA) monomers. To verify this mechanism further, we prepared for the third test a batch of PMMA particles (batch 6; N21; see Table 2) in a separate synthesis using a monomer mixture containing 5 wt % DMAE-MA monomer. We thus incorporated the DMAE-MA groups in PMMA via a different route.

We prepared suspensions of all six batches in CHB (for a comparison of sedimentation) or a solvent mixture of CHB and 20 wt % *cis*-decalin (for electrophoresis measurements) at a

volume fraction of $\eta \approx 0.02$. The experimental procedure and analysis were the same as described before; see Section 2. Additional experimental and analysis details can be found in the Supporting Information.

The charges and observed phase behavior for the six batches are summarized in Table 2; the corresponding confocal images are shown in Figure 3. We see that U29 and H29 had similar low and negative charges. The charge of T29, including the sign, was comparable to that of U29 and H29, but closer to zero. On the other hand, L29, S29, and N21 had larger positive charges. The phase behavior (Figure 3) reflected the measured charges. The phase behavior of U29, H29, and T29 (Figure 3a, c, e) is similar: all were fluid and had a small sediment height. In accordance with the higher charge, L29 was crystalline and had a sediment height equal to the height of the capillary (Figure 3b, g). The slightly lower charge of S29 resulted in a sediment with a lower height that contained three crystalline layers adjacent to the wall (Figure 3d, h). The phase behavior of the N21 particles (Figure 3f, i) was similar to that of the L29 particles (Figure 3b, g): at a volume fraction of $\eta \approx 0.02$ this system was crystalline and the sediment spanned the entire height of the capillary.

In contrast to unlocked particles U20 and U16 (Table 1), particle U29 had a negative charge. Apparently, the adsorption equilibria of positive and negative ions were different for U29, in such a way that the net charge was negative. At this point, we do not have a definite explanation for this difference. The similarity of the charge and behavior of particles U29 and H29

means simply heating the particles without the presence of DMAE (H29) did not result in a charge increase. In contrast, L29 and S29 showed a large increase in charge compared to U29, indicating that DMAE indeed played a role. Batch 4 (S29) was not only checked after 2 weeks, but also after 2 h of stirring, the same reaction time as used for the locking procedure (batch 2, L29). The phase behavior at this earlier point in time was similar to U29, H29, and T29 (fluid, small sediment height). Thus, stirring the locking reaction mixture for 2 h at room temperature (as for S29) did not result in a similar charge increase as stirring the locking reaction mixture at 130 °C (as for L29), despite the 10 times higher concentration of DMAE in the former case. This dependence on temperature indicates that attachment of DMAE took place by covalent bonding, for which we expect an activation energy and therefore a dependence on temperature, rather than adsorption, for which we do not expect a temperature dependence, since there is usually no energy barrier to overcome. Furthermore, the relatively high positive charge of N21 and its phase behavior being similar to L29 also indicate that the charge increase resulted from covalent bonding of DMAE to MAA monomers. Finally, the measured charge and phase behavior of T29 were comparable to those of U29 and H29, which is another indication that the large charge increase of L29 and S29 was primarily caused by covalent bonding of DMAE, not by adsorption, as in the latter case we would expect a similar charge increase with TEA. The less negative charge of T29, compared to U29 and H29, might be due to some adsorption of TEA. We note that TEA has a low dielectric constant ($\epsilon_r = 2.4$), in contrast to DMAE ($\epsilon_r = 17.18^{58}$), which means the possibility exists that adsorbed TEA was removed by washing with hexane, while DMAE was not. However, given the temperature-dependence of the rate of charge increase, we do not think that this was the case. We conclude that covalent bonding of DMAE was the dominant mechanism by which DMAE was incorporated into the particles.

As a final test, to find out whether the DMAE-MA ester can be formed in dodecane under the conditions of the locking procedure, we performed a test reaction between MAA and DMAE (molar ratio 1:1) under the same conditions. Infrared (IR) spectroscopy and electron spray ionization-mass spectrometry (ESI-MS) showed that under these conditions DMAE can bind covalently to MAA (see SI).

On the basis of our findings we recommend that the catalyst for the locking reaction should be carefully selected. To lock PMMA particles while at the same time increasing the particles' capability to acquire charge, alcohol or diol amines should be used, such as DMAE and diethanolamine.⁴³ To avoid affecting the particles' charging behavior, alkyl amines, such as TEA or *N,N*-dimethyldodecylamine,⁵⁹ should be used instead.

Because DMAE reacts with MA groups of the particle, the DMAE concentration decreases over time. However, since DMAE is present in excess (2–10 ×) compared to the number of MA groups in a 10-nm layer of PMMA at the surface of the particles, we expect that this concentration decrease will not affect the locking reaction. In the case that MA groups in the interior of the particle can also react, which cannot be completely ruled out at the increased temperature of 130 °C, the concentration decrease could be significant. We performed a test to verify the locking (see SI), and we concluded that the stabilizer was indeed covalently bonded to the PMMA particles.

4. CONCLUSIONS

We determined the size dependence of the dimensionless surface potential $\beta\psi_0$ and particle charge number Z in suspensions of PHSA-*g*-PMMA-stabilized poly(methyl methacrylate) (PMMA) particles in cyclohexyl bromide (CHB) with diameters in the range $\sigma = 1.18$ – 4.36 μm . From the conductivity of CHB, the Debye screening length κ^{-1} was estimated to be 6 μm . We performed electrophoresis measurements in homemade electrophoresis sample cells, using confocal microscopy to measure the particle velocity profiles, from which we obtained the electrophoretic mobility μ_E for each particle species, both for fluid samples and for samples which had formed colloidal crystals. To calculate $\beta\psi_0$ and Z from μ_E we employed the theoretical approach by Carrique et al.,⁴⁶ which takes into account double-layer overlap and uses a Kuwabara cell model to relate μ_E to $\beta\psi_0$ and Z for arbitrary κ^{-1} and volume fraction η by numerically solving the full Poisson–Boltzmann equation.

We used mostly locked particles (for which the stabilizer is covalently bonded to the particle surface), but also some unlocked particles (stabilizer adsorbed to the particle surface) for our measurements. We found that the locking state of the particles had a profound influence on their surface potential. For locked particles we found a surface potential independent of the size of the particle (a fit yields $\beta\psi_0 = 5.1 \pm 0.3$), and a (bare) particle charge that was proportional to the square of the diameter, corresponding to a surface charge density of roughly 47 ± 3 $e \mu\text{m}^{-2}$. Unlocked particles had a significantly lower surface potential and charge ($\beta\psi_0 \approx 3.3$ – 3.9) than locked particles ($\beta\psi_0 \approx 3.8$ – 6.8). We investigated this difference in more detail and found that the charge increase was due to chemical coupling of the locking catalyst 2-(dimethylamino)-ethanol (DMAE) to methacrylic acid groups in our PMMA, which were present at a low mass fraction (of a few %) to facilitate the locking of the comb-graft stabilizer. The chemical incorporation of amino groups is an interesting way to systematically increase the positive charge on our particles in low-polar solvents like CHB. We found small but significant shifts in particle charges when different spheres of roughly the same size were mixed.

In future work it would be interesting to systematically investigate the particle surface potential and charge as a function of the added amount of DMAE, including the possibility to tune the particle charge by varying the amount of DMAE. In addition, it would be interesting to extend the $\beta\psi_0$ -versus- σ and Z -versus- σ curves to even smaller and larger particle diameters than in the present work ($\sigma = 1.18$ – 4.36 μm), and to extend the research on mixtures of particles of different size to further investigate the changes in particle charge that occur upon mixing. Questions relating to the details of the particle interactions remain open—for example, how the charge is affected by the screening length, the solvent composition, and the adsorption of salts like TBAB, and how the particle interactions in binary mixtures can be described. To what extent the insights about the charging of this PMMA model system can be applied to other types of colloidal particles remains an open question as well.

■ ASSOCIATED CONTENT

Supporting Information

Background information on (1) the interaction potential and (2) the ion concentration in low-polar solvents. (3) Procedure

for estimating the Debye screening length. (4) Incorporation of RITC fluorescent dye. (5) Mobility profiles for all electrophoresis measurements. Background information and experimental details for the study of the charge increase upon locking: (6) locking reaction and esterification reaction, (7) IR and ESI-MS analysis. (8) Experimental details for the electrophoresis measurements in Table 2. (9) Locking test. (10) Unlabeled PMMA. This material is available free of charge via the Internet at <http://pubs.acs.org/>.

AUTHOR INFORMATION

Corresponding Authors

*E-mail: marjolein.vanderlinden@espci.fr.

*E-mail: a.vanblaaderen@uu.nl.

Present Address

[‡]EC2M, UMR Gulliver 7083 CNRS, ESPCI ParisTech, 10 rue Vauquelin, 75005 Paris, France.

Notes

The authors declare no competing financial interest.

ACKNOWLEDGMENTS

We thank Teun Vissers for providing the particle tracking algorithm and the cell model code by Félix Carrique and Angèl Delgado. Peter Helfferich is thanked for technical assistance and Emma Folkertsma is thanked for help with IR and ESI-MS analysis. Part of this work was supported by NWO-SRON. N.A.B. acknowledges the support of an IPP project with Shell and the Foundation for Fundamental Research on Matter (FOM). M.N.v.d.L. acknowledges the support of an NWO Top Talent grant from The Netherlands Organisation for Scientific Research (NWO).

REFERENCES

- (1) Russel, W. B.; Saville, D. A.; Schowalter, W. R. *Colloidal Dispersions*; Cambridge University Press: Cambridge, 1992.
- (2) van der Hoeven, Ph. C.; Lyklema, J. Electrostatic stabilization in non-aqueous media. *Adv. Colloid Interface Sci.* **1992**, *42*, 205–277.
- (3) Morrison, I. D. Electrical charges in nonaqueous media. *Colloids Surf., A* **1993**, *71*, 1–37.
- (4) Royall, C. P.; Leunissen, M. E.; van Blaaderen, A. A new colloidal model system to study long-range interactions quantitatively in real space. *J. Phys.: Condens. Matter* **2003**, *15*, S3581–S3596.
- (5) Leunissen, M. E.; Christova, C. G.; Hynninen, A.-P.; Royall, C. P.; Campbell, A. I.; Imhof, A.; Dijkstra, M.; van Roij, R.; van Blaaderen, A. Ionic colloidal crystals of oppositely charged particles. *Nature* **2005**, *437*, 235–240.
- (6) Bartlett, P.; Campbell, A. I. Three-dimensional binary superlattices of oppositely charged colloids. *Phys. Rev. Lett.* **2005**, *95*, 128302.
- (7) Leunissen, M. E.; van Blaaderen, A.; Hollingsworth, A. D.; Sullivan, M. T.; Chaikin, P. M. Electrostatics at the oil-water interface, stability, and order in emulsions and colloids. *Proc. Natl. Acad. Sci. U. S. A.* **2007**, *104*, 2585–2590.
- (8) Yethiraj, A.; van Blaaderen, A. A colloidal model system with an interaction tunable from hard sphere to soft and dipolar. *Nature* **2003**, *421*, 513–517.
- (9) Binks, B. P. Particles as surfactants – similarities and differences. *Curr. Opin. Colloid Interface Sci.* **2002**, *7*, 21–41.
- (10) Comiskey, B.; Albert, J. D.; Yoshizawa, H.; Jacobson, J. An electrophoretic ink for all-printed reflective electronic displays. *Nature* **1998**, *394*, 253–255.
- (11) Jenkins, P.; Basu, S.; Keir, R. I.; Ralston, J.; Thomas, J. C.; Wolffenbittel, B. M. A. The electrochemistry of nonaqueous copper phthalocyanine dispersions in the presence of a metal soap surfactant:

a simple equilibrium site binding model. *J. Colloid Interface Sci.* **1999**, *211*, 252–263.

(12) Hao, T. Electrorheological fluids. *Adv. Mater.* **2001**, *13*, 1847–1857.

(13) Roberts, G. S.; Sanchez, R.; Kemp, R.; Wood, T.; Bartlett, P. Electrostatic charging of nonpolar colloids by reverse micelles. *Langmuir* **2008**, *24*, 6530–6541.

(14) Leunissen, M. E. *Manipulating colloids with charges & electric fields*. Ph.D. thesis, Utrecht University: The Netherlands, 2007; available at <http://www.colloid.nl>.

(15) Vissers, T.; Imhof, A.; Carrique, F.; Delgado, A. V.; van Blaaderen, A. Electrophoresis of concentrated colloidal suspensions in low-polar solvents. *J. Colloid Interface Sci.* **2011**, *361*, 443–455.

(16) Smith, P. G., Jr.; Patel, M. N.; Kim, J.; Milner, T. E.; Johnston, K. P. Effect of surface hydrophilicity on charging mechanism of colloids in low-permittivity solvents. *J. Phys. Chem. C* **2007**, *111*, 840–848.

(17) Sainis, S. K.; Germain, V.; Mejean, C. O.; Dufresne, E. R. Electrostatic interactions of colloidal particles in nonpolar solvents: Role of surface chemistry and charge control agents. *Langmuir* **2008**, *24*, 1160–1164.

(18) Hsu, M. F.; Dufresne, E. R.; Weitz, D. A. Charge stabilization in nonpolar solvents. *Langmuir* **2005**, *21*, 4881–4887.

(19) Kitahara, A.; Satoh, T.; Kawasaki, S.; Kon-No, K. Specific adsorption of surfactants containing Mn or Co on polymer particles revealed by zeta-potential in cyclohexane. *J. Colloid Interface Sci.* **1982**, *86*, 105–110.

(20) Keir, R. I.; Suparno; Thomas, J. C. Charging behavior in the silica/aerosol OT/decane system. *Langmuir* **2002**, *18*, 1463–1465.

(21) Strubbe, F.; Beunis, F.; Marescaux, M.; Neyts, K. Charging mechanism in colloidal particles leading to a linear relation between charge and size. *Phys. Rev. E* **2007**, *75*, 031405.

(22) Kemp, R.; Sanchez, R.; Mutch, K. J.; Bartlett, P. Nanoparticle charge control in nonpolar liquids: Insights from small-angle neutron scattering and microelectrophoresis. *Langmuir* **2010**, *26*, 6967–6976.

(23) Roberts, G. S.; Woods, T. A.; Frith, W. J.; Bartlett, P. Direct measurement of the effective charge in nonpolar suspensions by optical tracking of single particles. *J. Chem. Phys.* **2007**, *126*, 194503.

(24) Guo, Q.; Lee, J.; Singh, V.; Behrens, S. H. Surfactant mediated charging of polymer particles in a nonpolar liquid. *J. Colloid Interface Sci.* **2013**, *392*, 83–89.

(25) Gacek, M.; Bergsman, D.; Michor, E.; Berg, J. C. Effects of trace water on charging of silica particles dispersed in a nonpolar medium. *Langmuir* **2012**, *28*, 11633–11638.

(26) Dukhin, A.; Goetz, P. Evolution of water-in-oil emulsion controlled by droplet-bulk ion exchange: acoustic, electroacoustic, conductivity and image analysis. *Colloids Surf., A* **2005**, *253*, 51–64.

(27) Espinosa, C. E.; Guo, Q.; Singh, V.; Behrens, S. H. Particle charging and charge screening in nonpolar dispersions with nonionic surfactants. *Langmuir* **2010**, *26*, 16941–16948.

(28) Smith, G. N.; Eastoe, J. Controlling colloid charge in nonpolar liquids with surfactants. *Phys. Chem. Chem. Phys.* **2013**, *15*, 424–439.

(29) Alexander, S.; Chaikin, P. M.; Grant, P.; Morales, G. J.; Pincus, P.; Hone, D. Charge renormalization, osmotic pressure, and bulk modulus of colloidal crystals: Theory. *J. Chem. Phys.* **1984**, *80*, 5776–5781.

(30) Vissers, T.; van Blaaderen, A.; Imhof, A. Band formation in mixtures of oppositely charged colloids driven by an ac electric field. *Phys. Rev. Lett.* **2011**, *106*, 228303.

(31) Vissers, T.; Wysocki, A.; Rex, M.; Löwen, H.; Royall, C. P.; Imhof, A.; van Blaaderen, A. Lane formation in driven mixtures of oppositely charged colloids. *Soft Matter* **2011**, *7*, 2352–2356.

(32) Israelachvili, J. N. *Intermolecular and Surface Forces*, 3rd ed.; Academic Press: Burlington, MA, 2011.

(33) Heston, W. M., Jr.; Hennelly, E. J.; Smyth, C. P. Dielectric constants, viscosities, densities, refractive indices and dipole moment calculations for some organic halides. *J. Am. Chem. Soc.* **1950**, *72*, 2071–2075.

- (34) Fuoss, R. M. Dependence of the Walden product on dielectric constant. *Proc. Natl. Acad. Sci. U. S. A.* **1959**, *45*, 807–813.
- (35) Miller, J. F.; Schätzel, K.; Vincent, B. The determination of very small electrophoretic mobilities in polar and nonpolar colloidal dispersions using phase analysis light scattering. *J. Colloid Interface Sci.* **1991**, *143*, 532–554.
- (36) Medebach, M.; Palberg, T. Phenomenology of colloidal crystal electrophoresis. *J. Chem. Phys.* **2003**, *119*, 3360–3370.
- (37) Medebach, M.; Shapran, L.; Palberg, T. Electrophoretic flow behaviour and mobility of colloidal fluids and crystals. *Colloids Surf., B* **2007**, *56*, 210–219.
- (38) Poovarodom, S.; Poovarodom, S.; Berg, J. C. Effect of alkyl functionalization on charging of colloidal silica in apolar media. *J. Colloid Interface Sci.* **2010**, *351*, 415–420.
- (39) Royall, C. P.; Leunissen, M. E.; Hynninen, A.-P.; Dijkstra, M.; van Blaaderen, A. Re-entrant melting and freezing in a model system of charged colloids. *J. Chem. Phys.* **2006**, *124*, 244706.
- (40) Hunter, R. J. *Zeta Potential in Colloid Science. Principles and Applications*; Academic Press, London, 1981.
- (41) Bosma, G.; Pathmamanoharan, C.; de Hoog, E. H. A.; Kegel, W. K.; van Blaaderen, A.; Lekkerkerker, H. N. W. Preparation of monodisperse, fluorescent PMMA-latex colloids by dispersion polymerization. *J. Colloid Interface Sci.* **2002**, *245*, 292–300.
- (42) Elsesser, M. T.; Hollingsworth, A. D. Revisiting the synthesis of a well-known comb-graft copolymer stabilizer and its application to the dispersion polymerization of poly(methyl methacrylate) in organic media. *Langmuir* **2010**, *26*, 17989–17996.
- (43) Antl, L.; Goodwin, J. W.; Hill, R. D.; Ottewill, R. H.; Owens, S. M.; Papworth, S.; Waters, J. A. The preparation of poly(methyl methacrylate) latices in non-aqueous media. *Colloids Surf.* **1986**, *17*, 67–78.
- (44) El Masri, D.; Vissers, T.; Badaire, S.; Stiefelhagen, J. C. P.; Vutukuri, H. R.; Helfferich, P.; Zhang, T. H.; Kegel, W. K.; Imhof, A.; van Blaaderen, A. A qualitative confocal microscopy study on a range of colloidal processes by simulating microgravity conditions through slow rotations. *Soft Matter* **2012**, *8*, 6979–6990.
- (45) Crocker, J. C.; Grier, D. G. Methods of digital video microscopy for colloidal studies. *J. Colloid Interface Sci.* **1996**, *179*, 298–310.
- (46) Carrique, F.; Arroyo, F. J.; Delgado, A. V. Electrokinetics of concentrated suspensions of spherical colloidal particles with surface conductance, arbitrary zeta potential, and double-layer thickness in static electric fields. *J. Colloid Interface Sci.* **2002**, *252*, 126–137.
- (47) Smallegang, F.; Boon, N.; Kater, M.; Dijkstra, M.; van Roij, R. Phase diagrams of colloidal spheres with a constant zeta-potential. *J. Chem. Phys.* **2011**, *134*, 074505.
- (48) Reinke, D.; Stark, H.; von Grünberg, H.-H.; Schofield, A. B.; Maret, G.; Gasser, U. Noncentral forces in crystals of charged colloids. *Phys. Rev. Lett.* **2007**, *98*, 038301.
- (49) Monovoukas, Y.; Gast, A. P. The experimental phase diagram of charged colloidal suspensions. *J. Colloid Interface Sci.* **1989**, *128*, 533–548.
- (50) Wette, P.; Schöpe, H. J.; Palberg, T. Comparison of colloidal effective charges from different experiments. *J. Chem. Phys.* **2002**, *116*, 10981–10988.
- (51) Stevens, M. J.; Falk, M. L.; Robbins, M. O. Interactions between charged spherical macroions. *J. Chem. Phys.* **1996**, *104*, 5209–5219.
- (52) Trizac, E.; Levin, Y. Renormalized jellium model for charge-stabilized colloidal suspensions. *Phys. Rev. E* **2004**, *69*, 031403.
- (53) Gisler, T.; Schulz, S. F.; Borkovec, M.; Sticher, H.; Schurtenberger, P.; D'Aguzzo, B.; Klein, R. Understanding colloidal charge renormalization from surface chemistry: Experiment and theory. *J. Chem. Phys.* **1994**, *101*, 9924–9936.
- (54) von Grünberg, H. H. Chemical charge regulation and charge renormalization in concentration colloidal suspensions. *J. Colloid Interface Sci.* **1999**, *219*, 339–344.
- (55) Zoetekouw, B. *Phase behaviour of charged colloids. Many-body effects, charge renormalization, and charge regulation*. Ph.D. thesis, Utrecht University: The Netherlands, 2006; available at <http://web.science.uu.nl/ITF/cmtscp/theses.htm>.
- (56) Royall, C. P.; van Roij, R.; van Blaaderen, A. Extended sedimentation profiles in charged colloids: the gravitational length, entropy, and electrostatics. *J. Phys.: Condens. Matter* **2005**, *17*, 2315–2326.
- (57) Butt, H.-J.; Graf, K.; Kappl, M. *Physics and Chemistry of Interfaces*; Wiley-VCH: Weinheim, Germany, 2006.
- (58) Sengwa, R. J.; Khatri, V.; Sankhla, S. Dielectric properties and hydrogen bonding interaction behaviour in binary mixtures of glycerol with amides and amines. *Fluid Phase Equilib.* **2008**, *266*, 54–58.
- (59) Klein, M. K.; Zumbusch, A.; Pfeleiderer, P. Photo-crosslinkable, deformable PMMA colloids. *J. Mater. Chem. C* **2013**, *1*, 7228–7236.